Supplementary Information (SI) for ChemComm.

Supporting Information

Pr_2O_3/RuO_2 Heterojunction Catalysts with Enhanced Activity and Durability for Acidic Oxygen Evolution

Jingya Han, Qi Xu, XinYi Xu, Jinjie Qian, Dong Cai, Huagui Nie, Xuemei Zhou, Zhi Yang**

Key Laboratory of Carbon Materials of Zhejiang Province, Institute of Industrial Carbon Materials and Hydrogen Energy Technology of Wenzhou University, Wenzhou University, Wenzhou 325035, China

E-mail: zxm.mei@163.com; yang201079@126.com

Experimental Section

1.1 Materials

Praseodymium nitrate hexahydrate purchased from Aladdin; Hexamminoruthenium(III) chloride hydrate (≥ 98%) purchased from Bide Pharmaceutical; Ruthenium(IV) dioxide RuO_2 (≥ 99.9%) and Iridium(IV) dioxide IrO_2 (≥ 99.9%) purchased from Aladdin; Hydrochloric acid (≥ 36%) and sulfuric acid (≥ 98%) were purchased from Zhejiang Zhongxing Chemical Reagent Co., Ltd. All chemicals were used without further purification.

1.2 Catalyst Preparation

Pr_2O_3/RuO_2 was synthesized via a one-step hydrothermal method. First, a 10 × 10 cm titanium felt sheet was cut into 1 × 2 cm pieces. These were ultrasonically cleaned for 20 minutes each in acetone, ethanol, and deionized water to remove surface oils and oxide layers, then dried in a vacuum oven to complete pretreatment. Titanium felt etching was then performed: An 18 wt% HCl solution was prepared. The titanium felt and 5 mL of this solution were added to a reactor, heated at 90°C for 15 minutes, cooled to room temperature, and the titanium felt was removed. It was rinsed multiple times with deionized water and vacuum-dried to obtain etched titanium felt (Ti-etching). Dissolve hexaammineruthenium chloride and praseodymium nitrate in a molar ratio of 5:3 in deionized water. Ultrasonicate for 30 minutes to ensure complete dispersion. Subsequently, add 3 wt% hydrochloric acid to the solution, bringing the total volume to 5 mL. Stir vigorously for 3 hours. After the reaction, transfer the precursor solution to a reactor vessel and immerse a piece of the etched titanium felt. The reactor was sealed and reacted at 180°C for 20 hours. After natural cooling to room temperature, the titanium felt was removed, rinsed three times with deionized water, and finally dried overnight in a vacuum oven at 60°C to obtain the Pr_2O_3/RuO_2 material. For comparison,

Pr_2O_3/RuO_2 samples with Ru:Pr molar ratios of 5:2 and 5:4 were prepared using the same method, labeled as Pr_2O_3/RuO_2 (5:2) and Pr_2O_3/RuO_2(5:4), respectively.

The synthesis of the control samples proceeded as follows: In situ-grown RuO_x was prepared using etched titanium felt under identical conditions without adding praseodymium nitrate. In situ-grown PrO_x was prepared using etched titanium felt under identical conditions without adding hexaammineruthenium chloride. Additionally, 4 mg of commercial RuO_2 was mixed with 1 mL of water and sonicated for 1 h. A 10 μL drop of this dispersion was applied onto carbon paper, dried, and then 5 μL of 0.2% naphthol solution was added dropwise. After drying, the reference catalyst com-RuO_2 was obtained. The com-IrO_2 catalyst was prepared using the same method for performance comparison.

1.3 Characterization of Pr_2O_3/RuO_2 Catalyst Materials

X-ray diffraction (XRD) patterns were obtained using Cu Kα radiation (40 kV, 100 mA, λ = 1.54056 Å) with a D/MAX-2400 diffractometer. Scanning electron microscopy (SEM) images and energy-dispersive X-ray spectroscopy (EDS) images were obtained using a JSM-6700 (spot 3.0, 15 kV). Transmission electron microscopy (TEM) and high-resolution transmission electron microscopy (HRTEM) were performed using a JEOL-2100F instrument (200 kV). X-ray photoelectron spectroscopy (XPS) measurements were performed using an ultra-high vacuum system equipped with a monochromatic Al-Kα X-ray source (10 mA, 15 kV) and a high-resolution GammaData-Scienta SES 2002 analyzer. Raman spectra were recorded at 532 nm using an Ar ion laser on a Renishaw in Via Raman microscope. Infrared measurements were performed using an IS50 Thermo Fisher infrared spectrometer.

1.4 Electrochemical Measurements

All electrochemical tests were conducted using a three-electrode system with a saturated calomel electrode (SCE) as the reference electrode and a platinum mesh as the counter electrode, employing a CHI 760E electrochemical workstation (CH Instrument Inc.). The working electrode was prepared by clamping the fabricated noble metal catalyst between platinum foil electrodes. The electrolyte solution was 0.5 M H_2SO_4. The saturated calomel electrode (SCE) was calibrated using a reversible hydrogen electrode (RHE) with $E_{vs.RHE} = E_{vs.SCE} + 0.256$ V. The overpotential η was calculated as $\eta = E_{vs.RHE} - 1.23$ V. Linear sweep voltammetry (LSV) was recorded over the potential range of 0.9 V to 1.4 V (vs. SCE) at a scan rate of 10 mV s^{-1}. LSV data compensated for 90% of the iR drop. The Tafel curves were calculated using the equation $\eta = b \log j + a$, where $b = 2.303RT/\alpha F$. In this expression, η represents the overpotential, a is the intercept, b denotes the Tafel slope, j refers to the current density, α is the charge transfer coefficient, T is the thermodynamic temperature, and F is the Faraday constant. All data originated from LSV. Electrochemical impedance spectroscopy (EIS) is an important tool for rapidly evaluating the activity of electrocatalysts: measuring and comparing the charge transfer resistance (Rct) at open-circuit voltage (OCP)—the smaller the Rct, the higher the activity typically is; whereas in situ EIS is performed at various potentials before and after the onset potential of the oxygen evolution reaction (OER) over a frequency range of 0.1 Hz to 100 kHz, enabling further analysis of the electrochemical behavior during the reaction process. Time-potential measurements were conducted at 10 mA cm^{-2} for 100 h, and multiple current steps (ISTEP) were performed at different current densities (10, 20, 30, 40, 50 mA cm^{-2}) to evaluate the stability of the prepared electrocatalyst. Cyclic stability test of the catalyst: continuous scanning for thousands to tens of thousands of cycles (10,000–20,000 cycles) at a fixed scan rate, followed by comparison of the polarization decay in the LSV curves before and after the scanning.

1.5 Details of Electrochemical Surface Area calculations

The ECSA was estimated from the electrochemical double-layer capacitance of the catalytic surface. The double-layer capacitance (C_{dl}) of the catalyst was determined via cyclic voltammetry (CV) within the non-Faradaic potential range of 0.95 to 1.15 V vs RHE, at scan rates (v) of 10, 20, 30, 40, 50, and 60 mV s^{-1}) to calculate the electrochemical surface area (ECSA) in 0.5 M H_2SO_4 solution. (C_{dl}) is estimated by plotting the difference between anodic and cathodic current densities versus scan rate. ECSA was estimated from C_{dl} using the formula: ECSA = S × C_{dl}/C_s[1], where S and C_s (0.04 mF cm^{-2}) represent the geometric area and specific capacitance of the working electrode, respectively.

1.6 Mass activity (MA) calculations

Mass activity (MA) is a physical quantity representing the apparent activity of precious metal catalysts. It is the MA apparent activity normalized by the mass of catalyst loaded on the electrode.

$$MA = \frac{j \times A}{m}$$

In the formula, MA represents the mass activity (A g^{-1}), j denotes the current density (A cm^{-2}), A signifies the effective area of the electrode (cm^2), and m stands for the catalyst loading mass (g). It reflects the utilization rate of precious metal per unit mass and serves as a crucial indicator for evaluating the economic efficiency of catalysts. Under identical testing conditions, a higher mass activity indicates better catalytic performance and lower material cost, making it suitable for comparing the performance of precious metal-based catalysts.

1.7 Turnover frequency (TOF) calculations

Turnover frequency (TOF) describes the intrinsic activity of a catalyst, i.e., the number of reactions occurring at a single active site within the reaction time. A higher TOF value indicates better catalyst performance and can be used to compare the activity among materials. However, because the structure of surface active centers is difficult to accurately analyze, the number of active sites cannot be determined. Typically, the total amount of catalyst is used to determine the number of active sites for the reaction, leading to a systematic underestimation of the TOF value. Nevertheless, this value can reflect the relative activity of the catalyst. The formula for calculating TOF is:

$$TOF = \frac{j \times A}{n \times F \times M}$$

j represents the current density, A denotes the surface area of the working electrode, n signifies the number of electrons required for the catalyst to undergo reaction (4 in OER), F stands for Faraday's constant, and M indicates the molar amount of the reactive species on the electrode. All data are obtained from LSV.

1.8 Apparent Activation Energy

To extract the apparent activation energy (E_{app}) of the acidic OER in 0.5 M sulfuric acid solution. LSV was measured at different temperatures (20°C, 30°C, 40°C, 50°C, 60°C). For heterogeneous catalytic reactions, the current density can be expressed as the apparent activation energy (E_{app}) in the Arrhenius equation. Here, A_{app} is the apparent pre-exponential factor, R is the ideal gas constant (8.314 J K^{-1} mol^{-1}), and T is the temperature in Kelvin. (K).

$$\frac{\partial(log j)}{\partial(\frac{1}{T})} = - \frac{E_{app}}{2.303R}$$

1.9 In-situ Raman Testing

Raman spectra were collected using a 532 nm laser on the aforementioned confocal Raman microscope under potential control from an electrochemical workstation. In brief, the cell was self-assembled using polytetrafluoroethylene (PTFE), with a circular quartz glass window protecting the objective lens. A Pr_2O_3/RuO_2-modified Au electrode served as the working electrode, while Pt wire and Ag/AgCl electrodes functioned as the counter and reference electrodes, respectively. The working electrode surface was positioned approximately 1 mm from the glass window. In-situ Raman measurements were performed on a Renishaw inVia Raman spectrometer controlled by WIRE 4.0 software. A 532 nm, 50 mW laser was vertically transmitted through the glass and focused onto the electrode surface using a 20× objective lens. The average acquisition time per spectrum was 5 minutes.

1.10 In-situ Infrared Testing

In-situ FTIR measurements were performed using a Thermo Fisher infrared spectrometer. The three-port sample cell consisted of a main body made of high-purity SiO_2 and a transparent window made of CaF_2. A Pr_2O_3/RuO_2-modified Au electrode served as the working electrode, with a Pt mesh and calomel electrode acting as counter and reference electrodes, respectively. The electrolyte was 0.5 M sulfuric acid solution. After sealing the cell, it is connected to the infrared spectrometer. Nitrogen gas is introduced, and liquid nitrogen is loaded to maintain a constant cooling temperature for the spectrometer. After 2 hours, background correction is performed using OMNIC software. Under potential control from the electrochemical workstation, spectra are acquired at different potentials, with an average acquisition time of 3 minutes per spectrum.

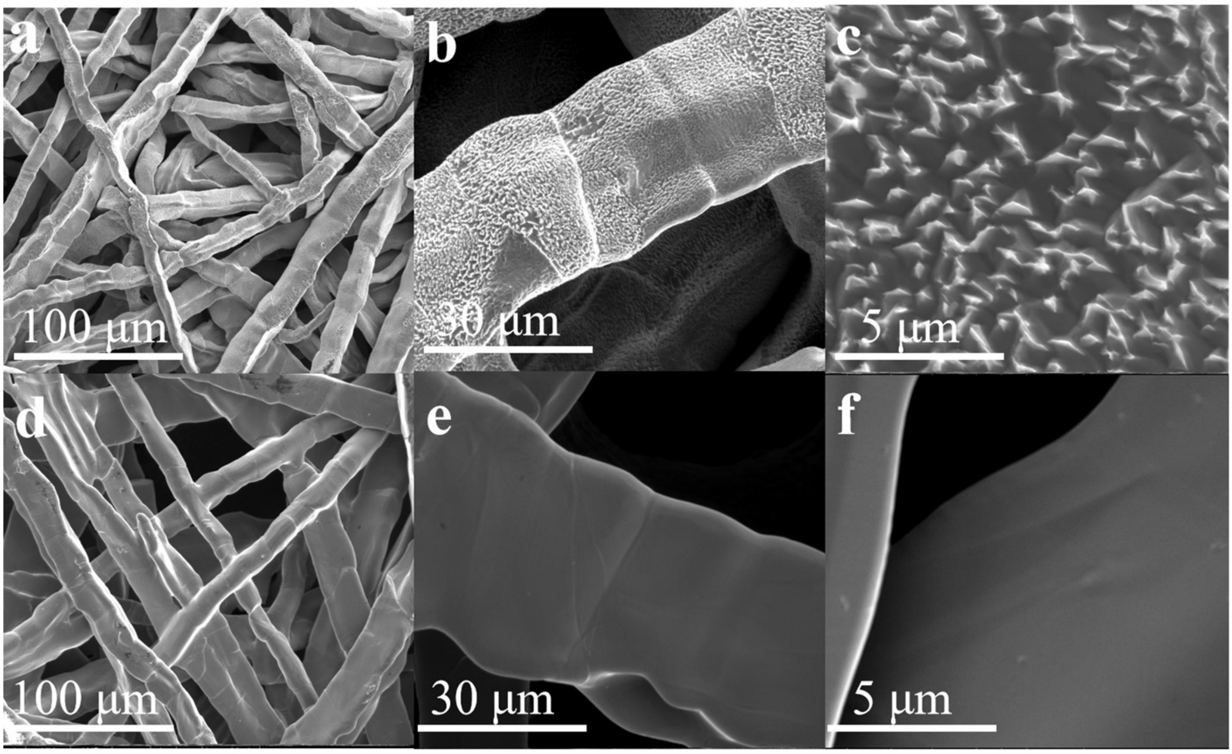

Fig. S1 a-c) SEM images of Ti-etching; d-f) SEM images of Ti-felt.

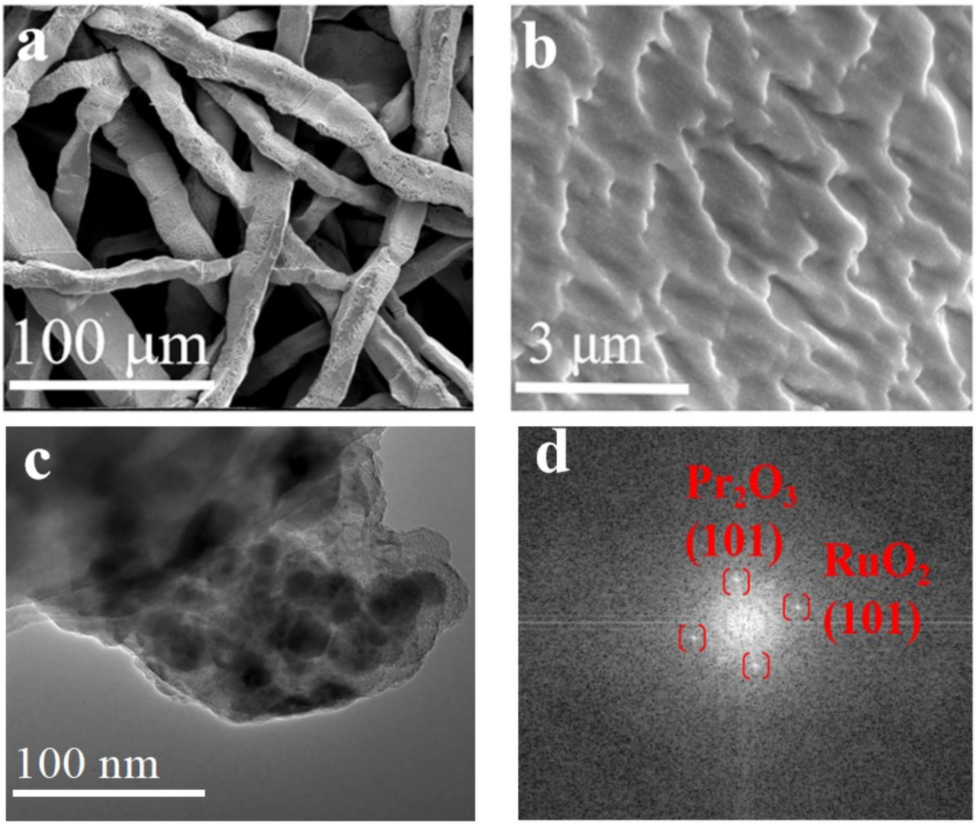

Fig. S2 SEM images (a and b) , TEM image (c) and crystal plane diagram (d) of Pr_2O_3/RuO_2.

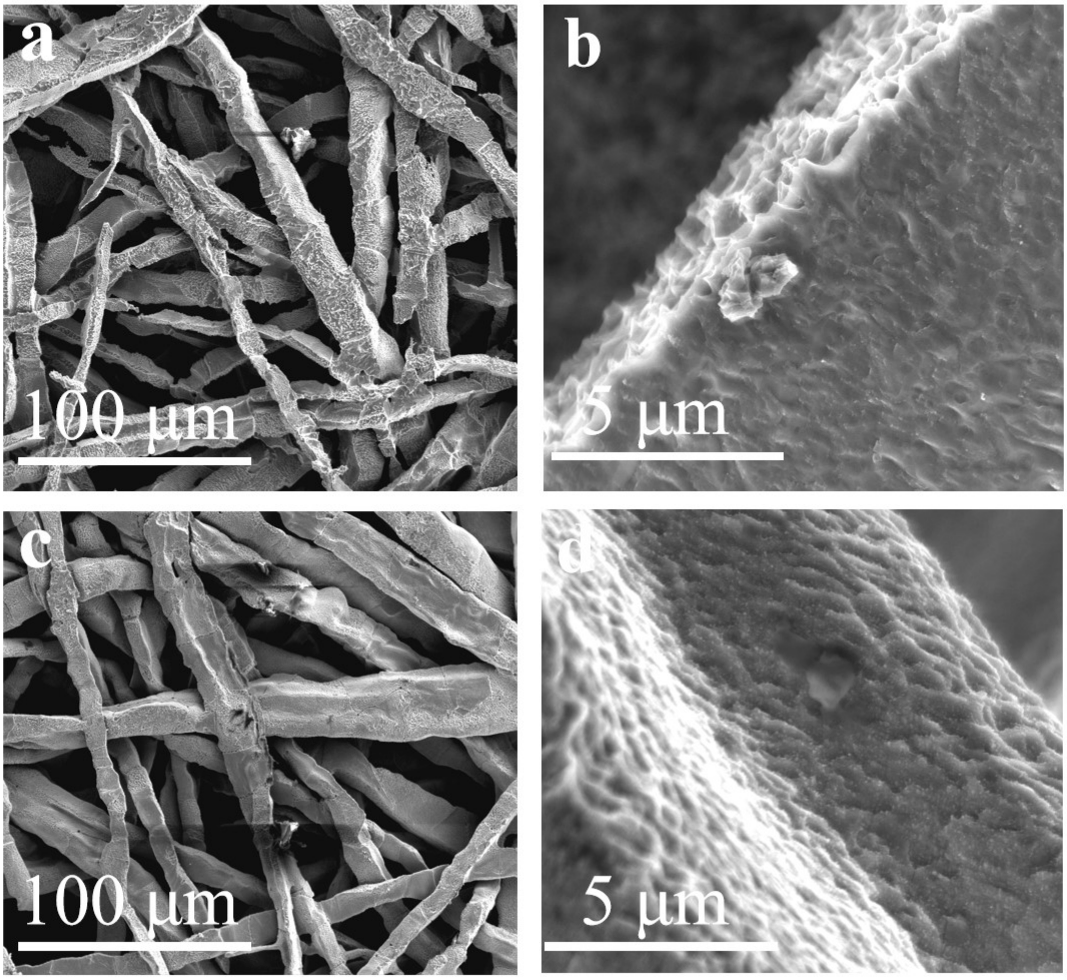

Fig. S3 a-b) SEM images of RuO_x; c-d) SEM images of PrO_x.

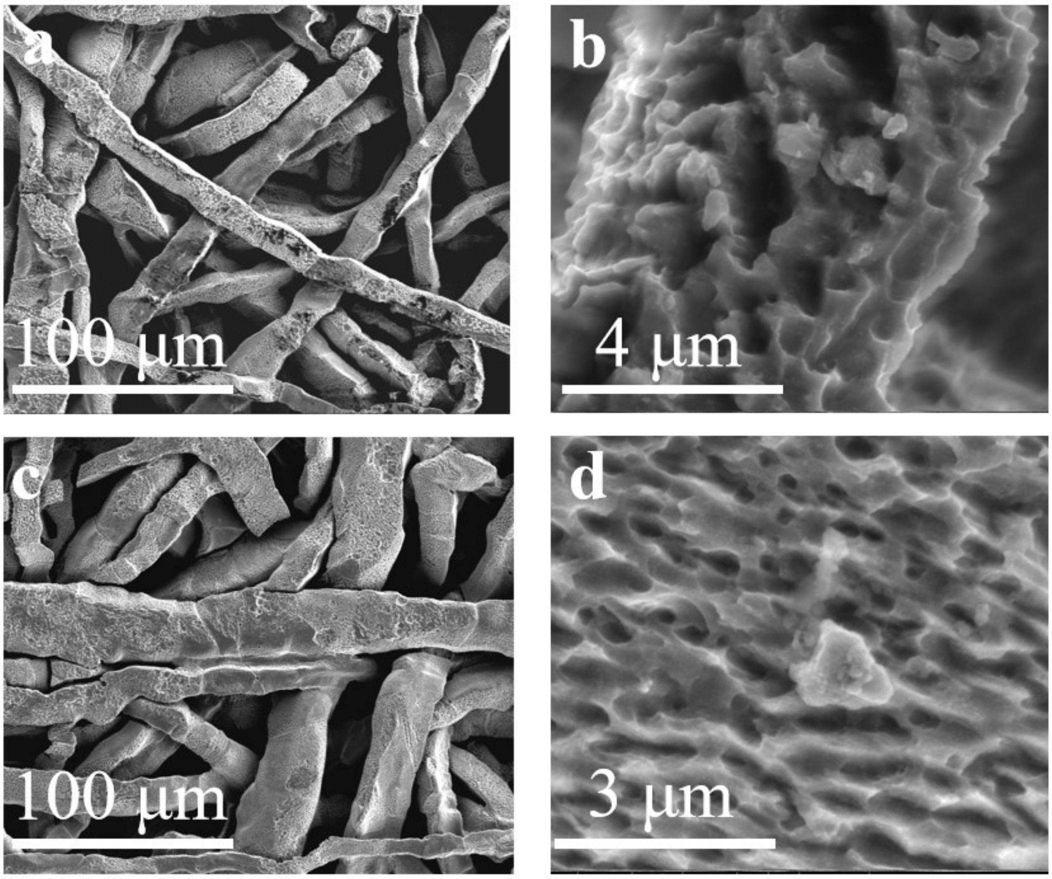

Fig. S4 a-b) SEM images of Pr_2O_3/RuO_2 (5:2); c-d) SEM images of Pr_2O_3/RuO_2 (5:4).

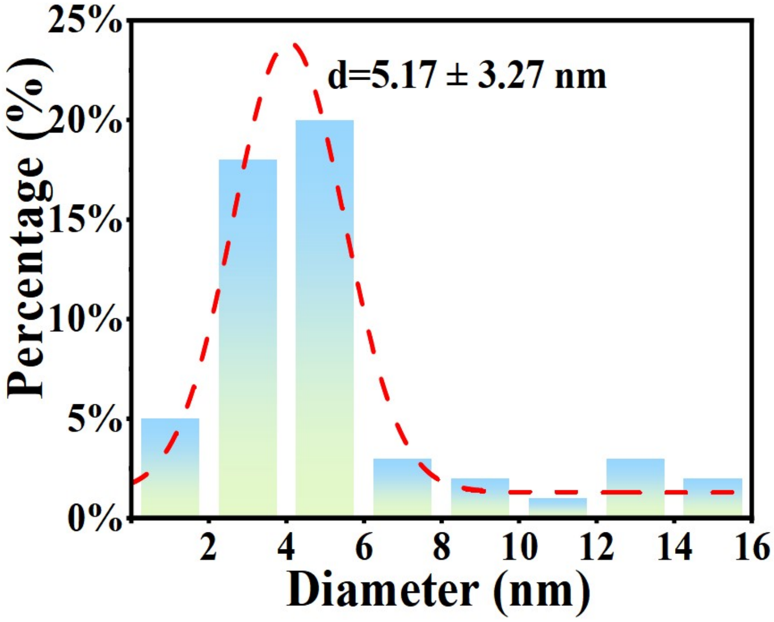

Fig. S5 shows the corresponding grain sizes of Pr_2O_3/RuO_2.

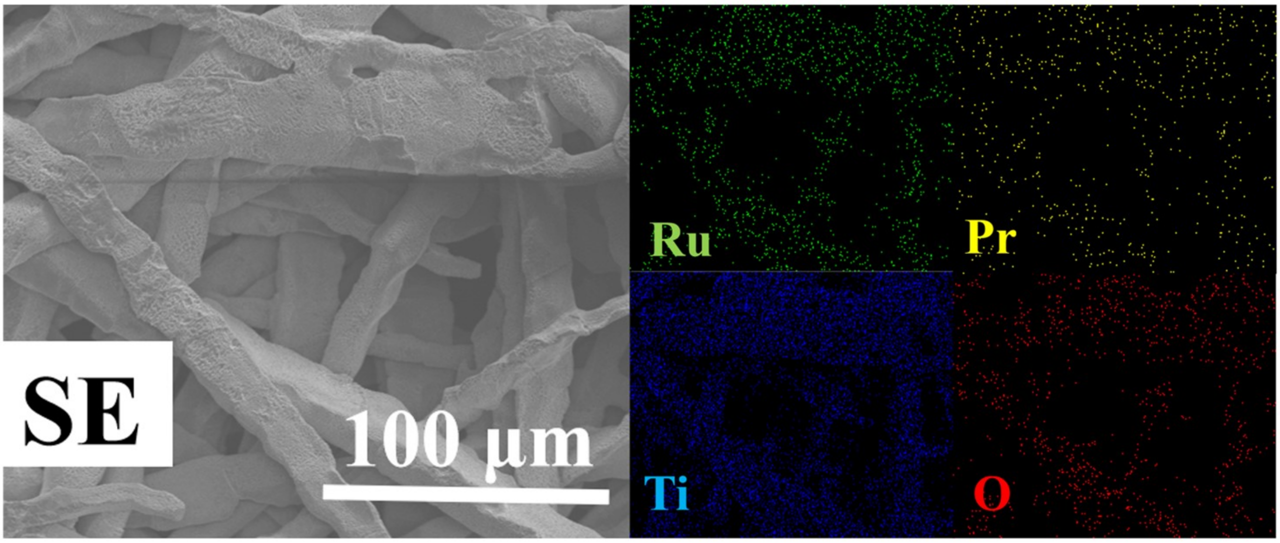

Fig. S6 Corresponding elemental mapping images of Ru, Pr, Ti, and O in Pr_2O_3/RuO_2 (Ru: green, Pr: yellow, Ti: blue, O: red).

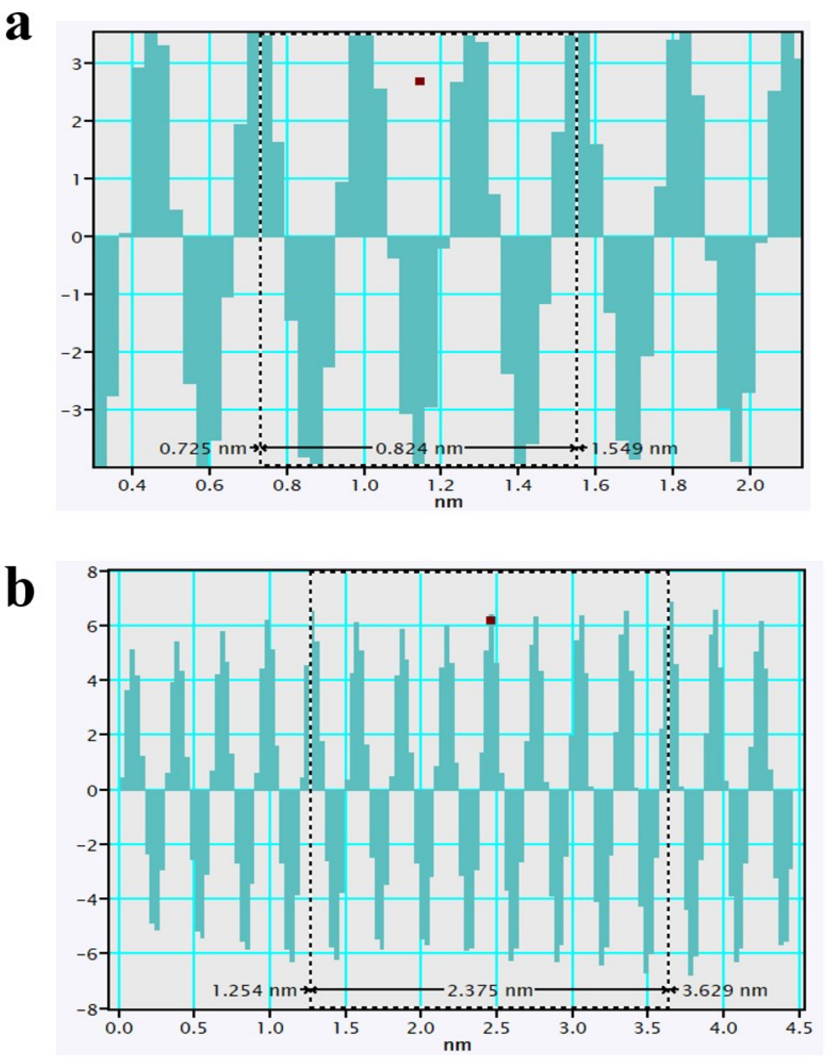

Fig. S7 a) shows the corresponding intensity coefficients and fringe spacings for RuO_2; b) shows the corresponding intensity coefficients and fringe spacings for Pr_2O_3.

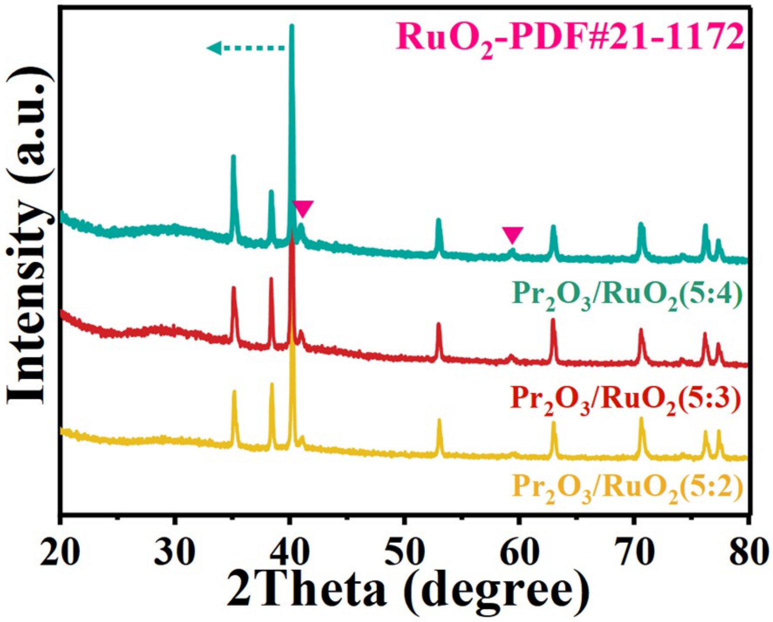

Fig. S8 XRD comparison patterns of Pr_2O_3/RuO_2 catalysts at different molar ratios.

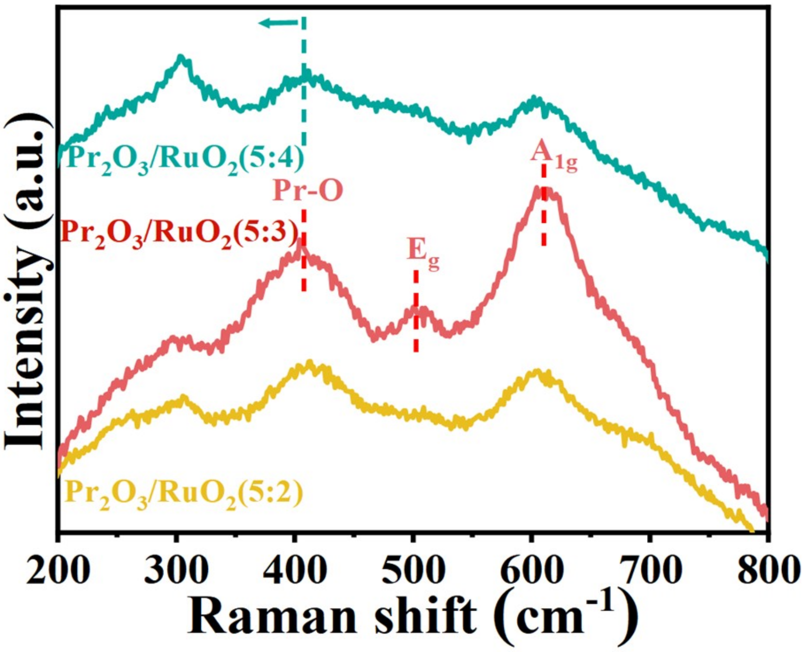

Fig. S9 Raman comparison spectra of Pr_2O_3/RuO_2 catalysts at different molar ratios.

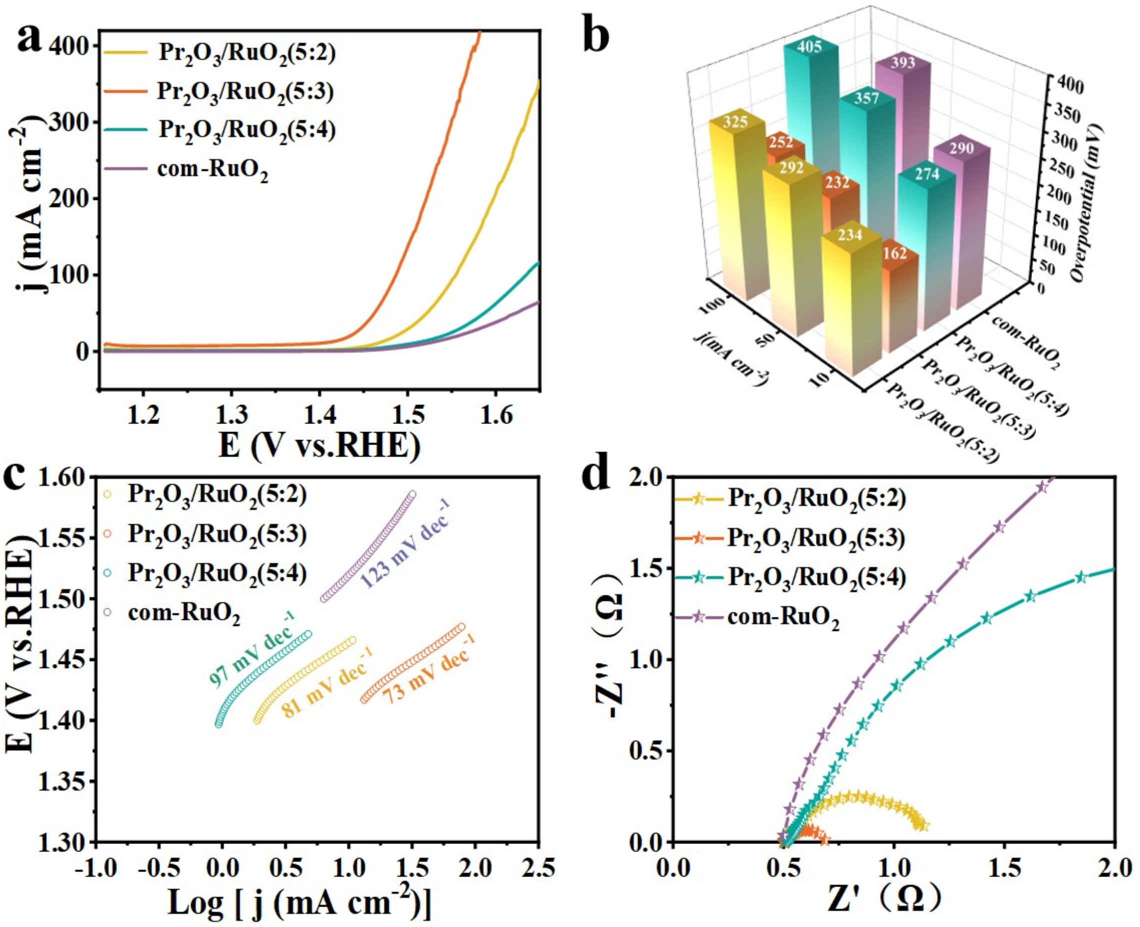

Fig. S10 Catalysts with different Pr_2O_3/RuO_2 ratios. a) LSV curve; b) Overpotential comparison at different current densities of 10 mA cm^{-2}, 50 mA cm^{-2}, and 100 mA cm^{-2}; c) Tafel curve calculated from (a); d) Electrochemical impedance spectrum at open circuit potential.

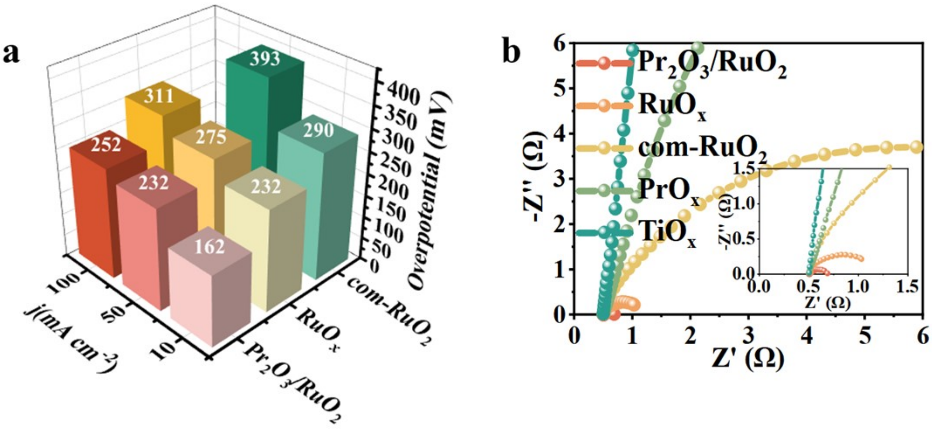

Fig. S11 a.Overpotential comparison of different catalysts at various current densities; b. EIS comparison of different catalysts at open circuit potential.

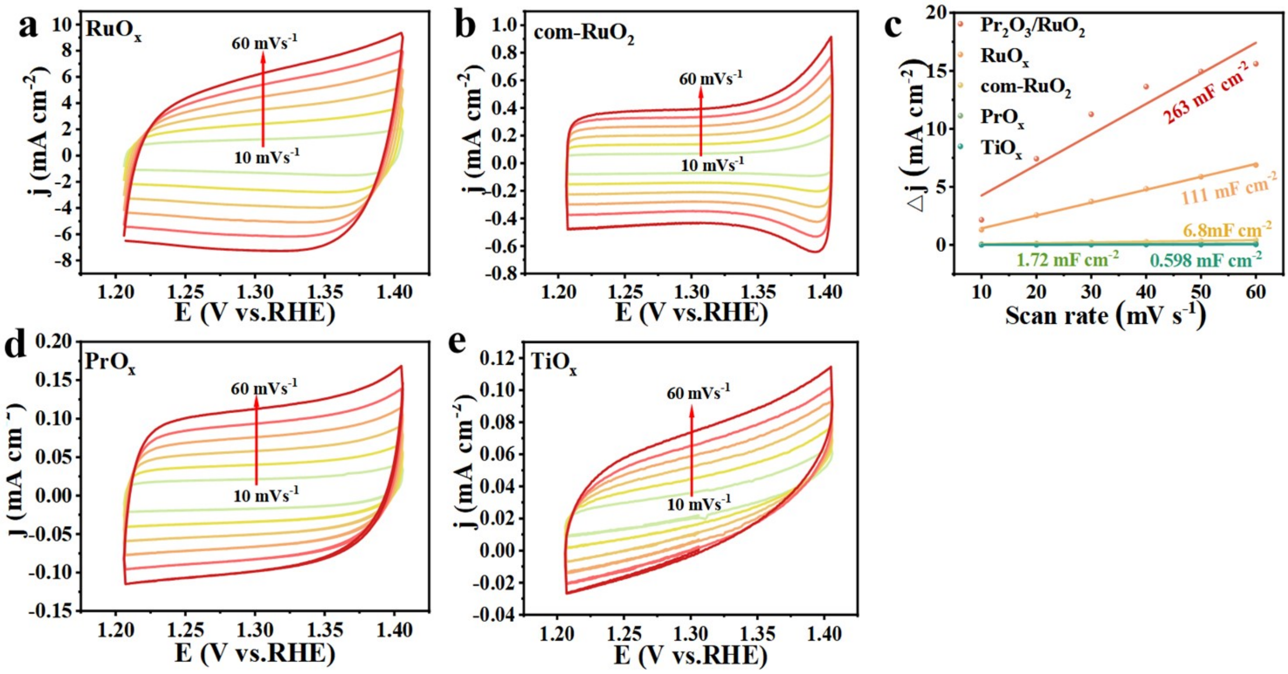

Fig. S12 a) CV curves of RuO_x; b) com-RuO_2; d) PrO_x; e) TiO_x catalysts; c) C_{dl} comparison diagram.

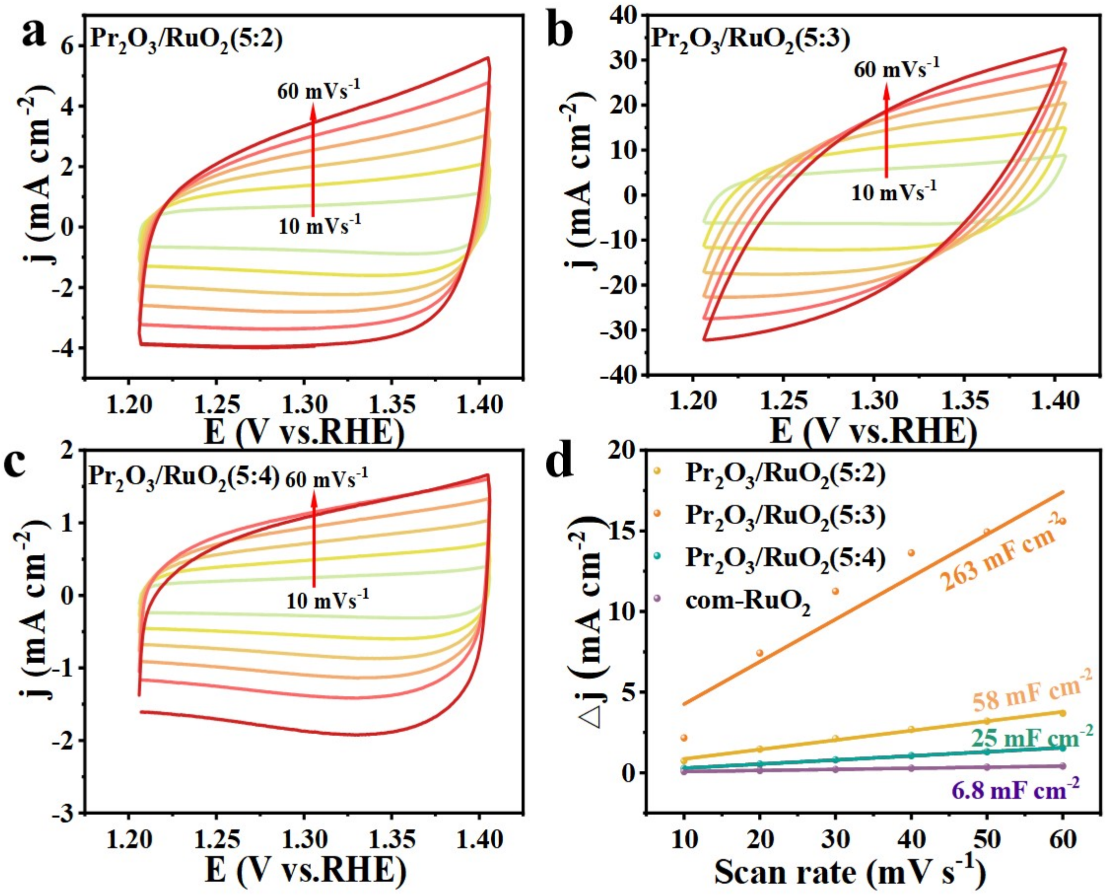

Fig. S13 a-c) Cyclic voltammetry (CV) curves of catalysts with different Pr_2O_3/RuO_2 ratios; d) Comparison chart of C_{dl}.

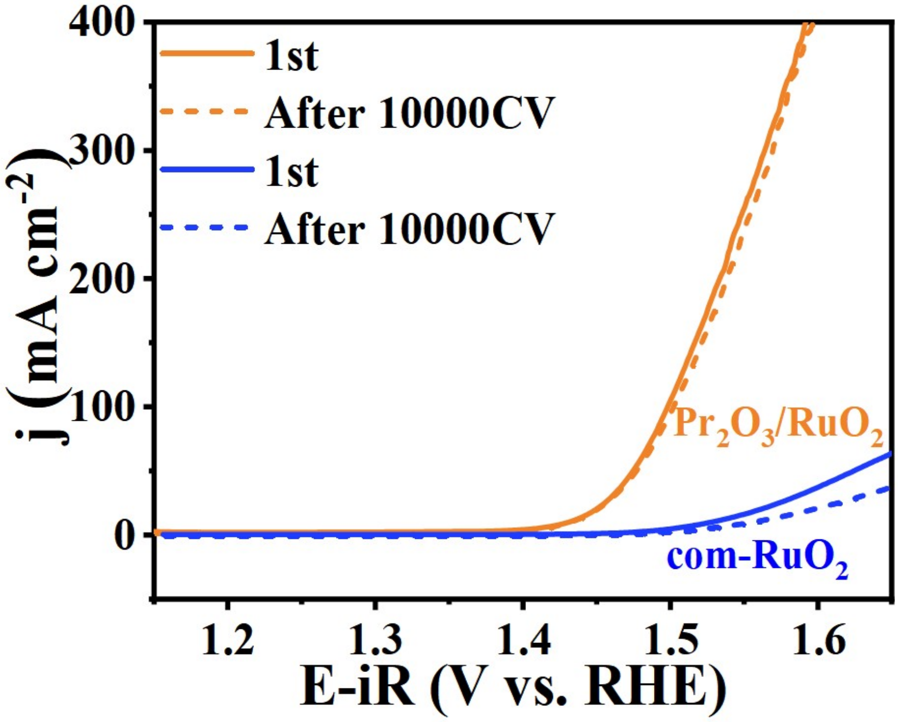

Fig. S14 LSV curves of Pr_2O_3/RuO_2 and commercial RuO_2 after 10,000 CVs cycles.

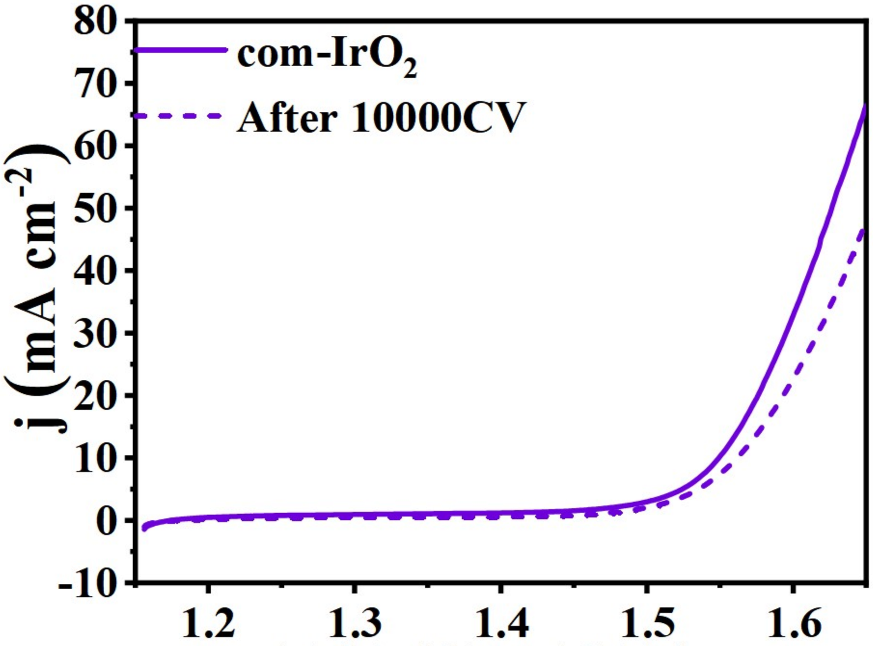

Fig. S15 LSV curve of commercial IrO_2 after 10,000 CV cycles.

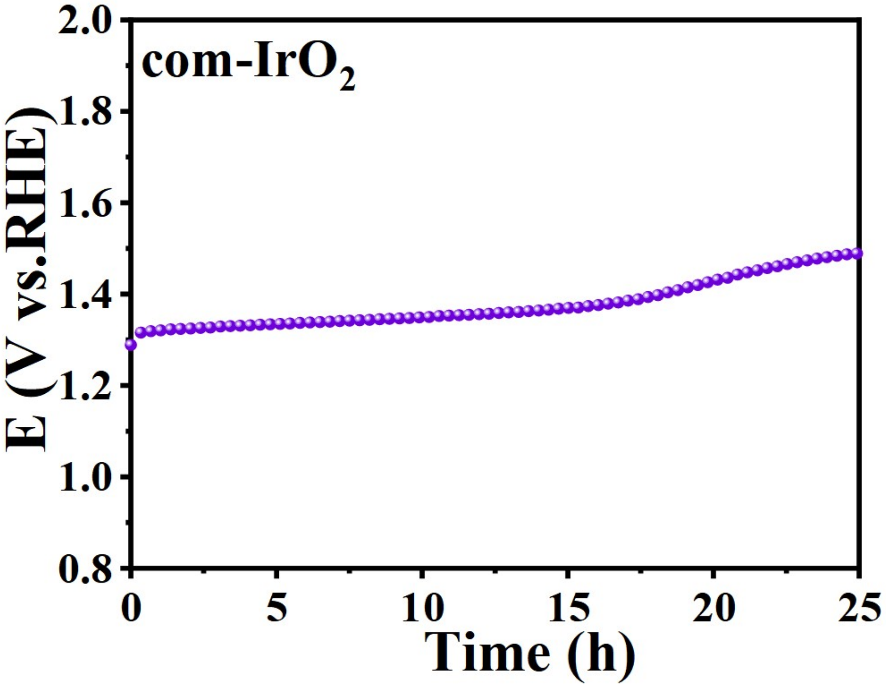

Fig. S16 Stability diagram of commercial IrO$_2$ at a current density of 10 mA cm^{-2}.

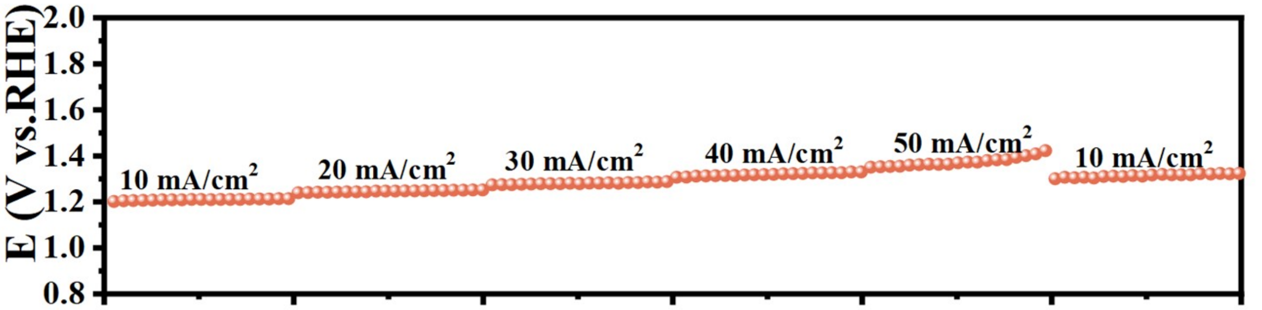

Fig. S17 Stability plots for the multi-step current method at 10, 20, 30, 40, 50 and 10 mA cm^{-2}.

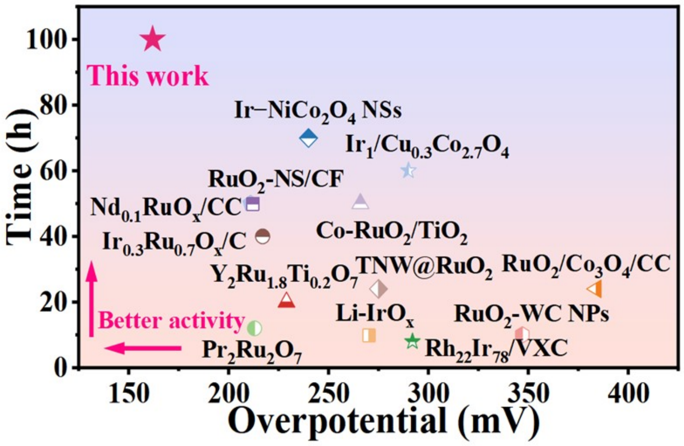

Fig. S18 Comparison of activity stability with other literature materials.

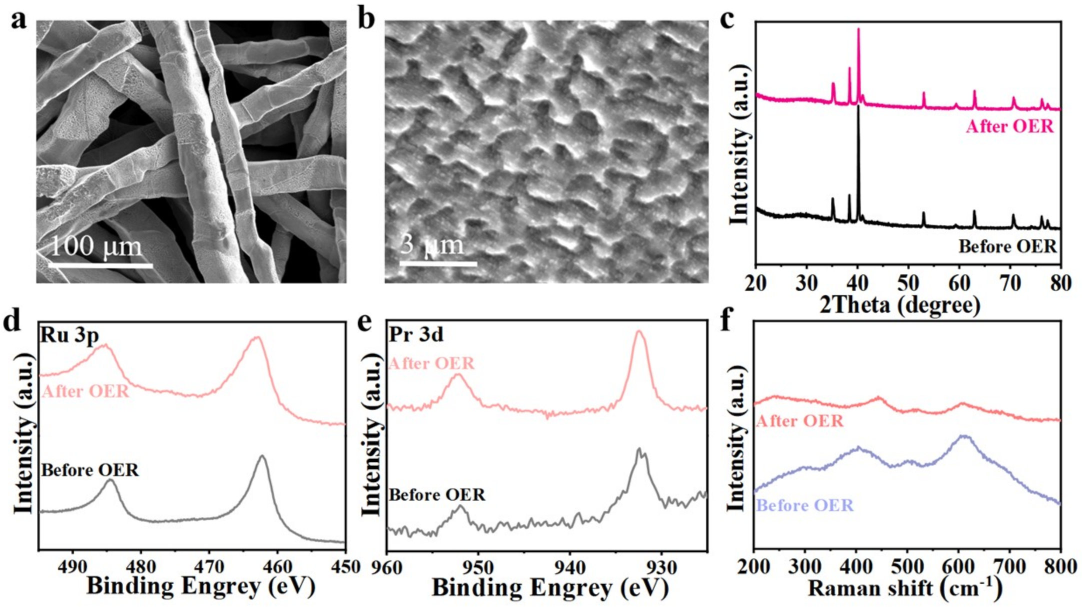

Fig. S19 Post-characterization of Pr_2O_3/RuO_2. (a) and (b) SEM images of Pr_2O_3/RuO_2 after stability testing; (c) XRD pattern of Pr_2O_3/RuO_2 after stability testing; (d) and (e) XPS spectra of Ru 3p and Pr 3d after stability testing; (f) Raman spectrum of Pr_2O_3/RuO_2 after stability testing.

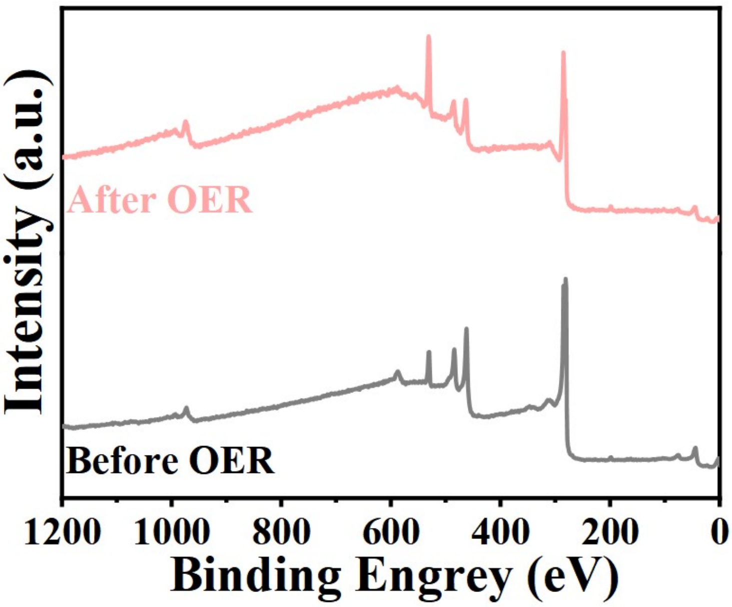

Fig. S20 Full XPS spectrum of Pr_2O_3/RuO_2 after characterization.

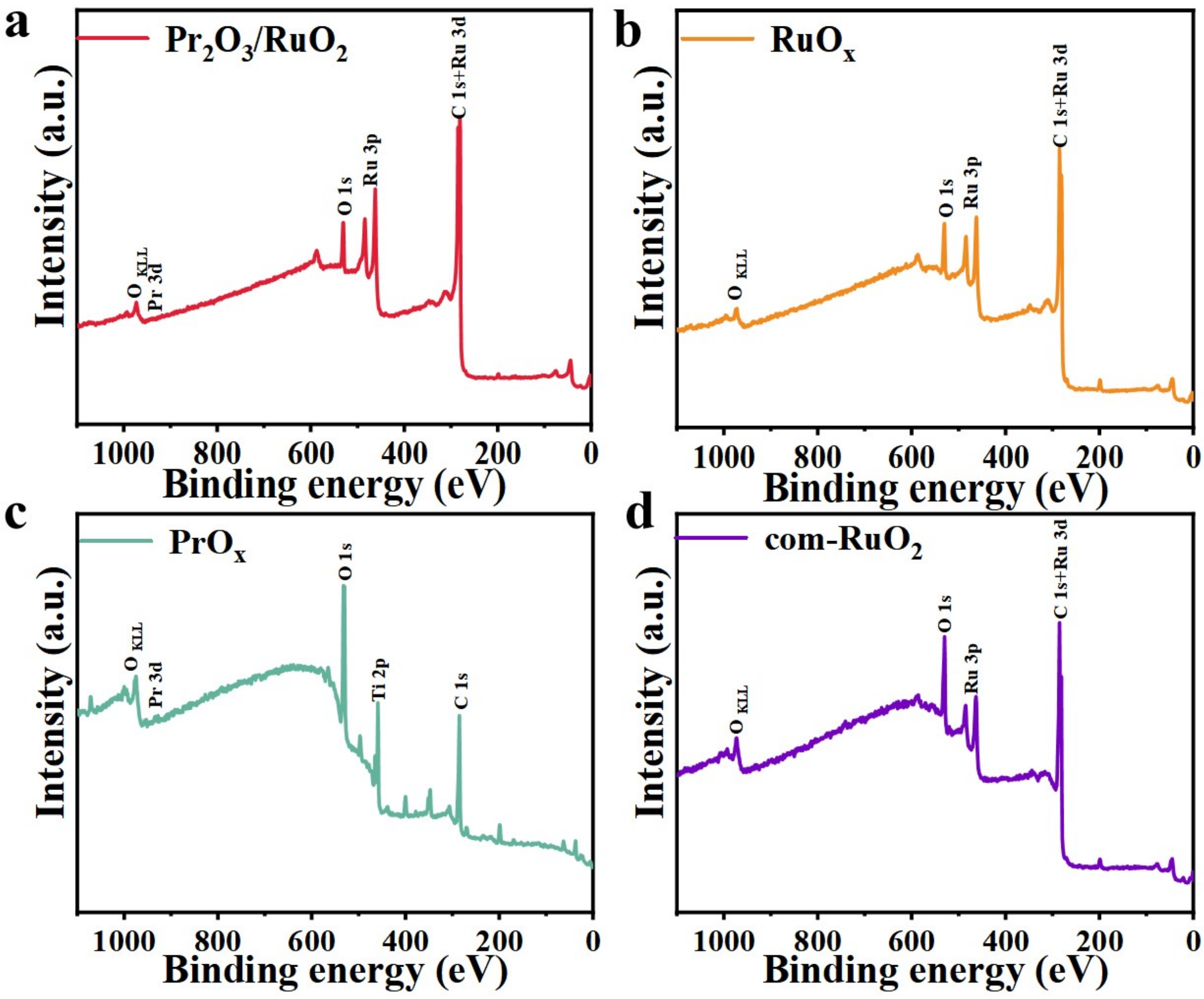

Fig. S21a) Full XPS spectrum of the Pr_2O_3/RuO_2 catalyst; b) Full XPS spectrum of the RuO_x catalyst; c) Full XPS spectrum of the PrO_x catalyst; d) Full XPS spectrum of the com-RuO_2 catalyst.

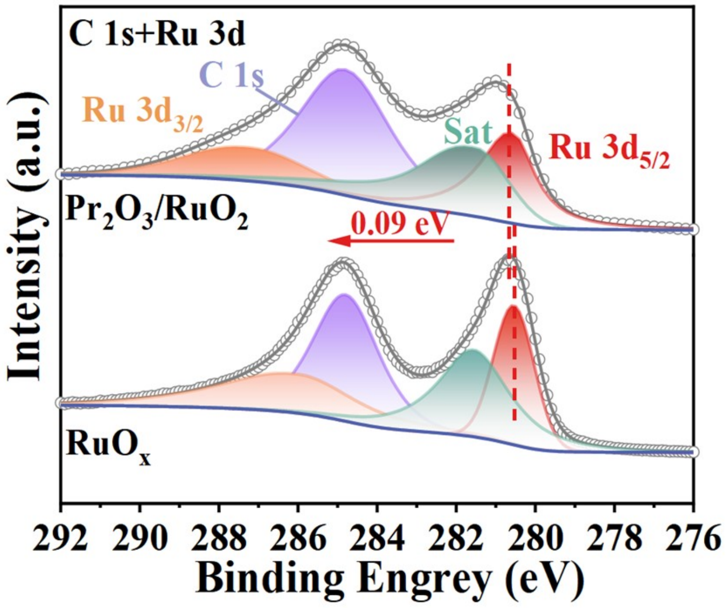

Fig. S22 XPS spectrum of Pr_2O_3/RuO_2 catalyst showing C 1s + Ru 3d.

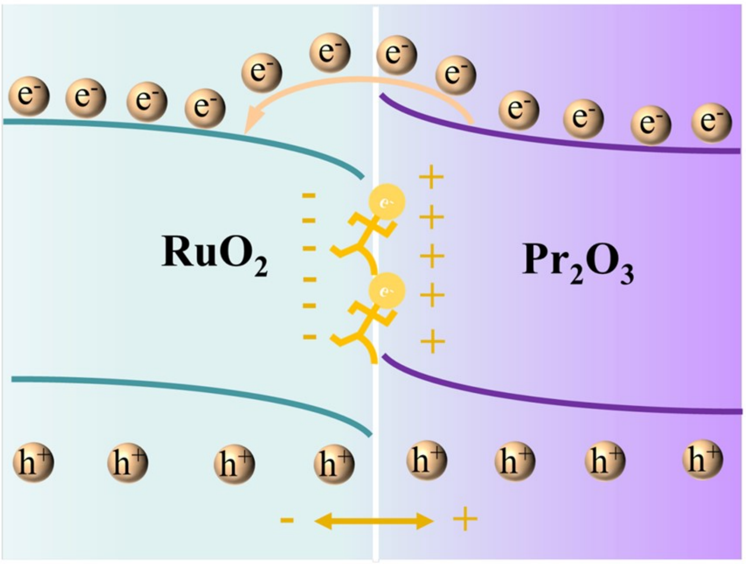

Fig. S23 Electronic transition diagram of Pr_2O_3/RuO_2.

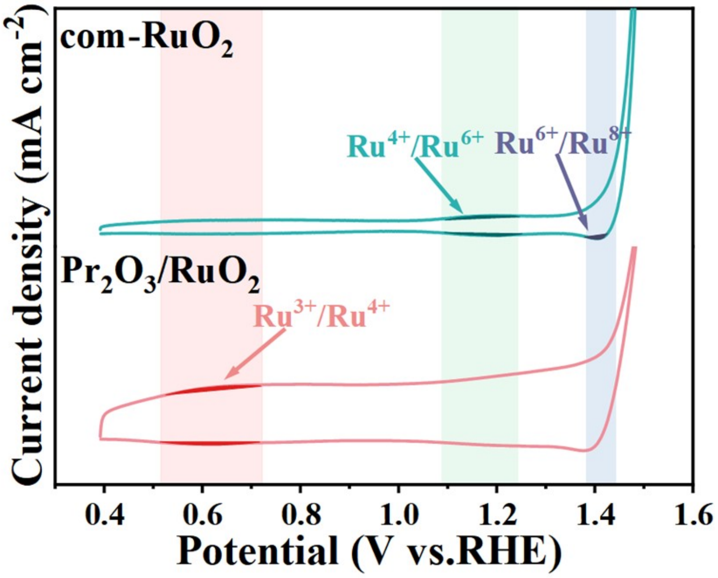

Fig. S24 Schematic diagram of different Ru oxidation states on the Pr_2O_3/RuO_2 catalyst.

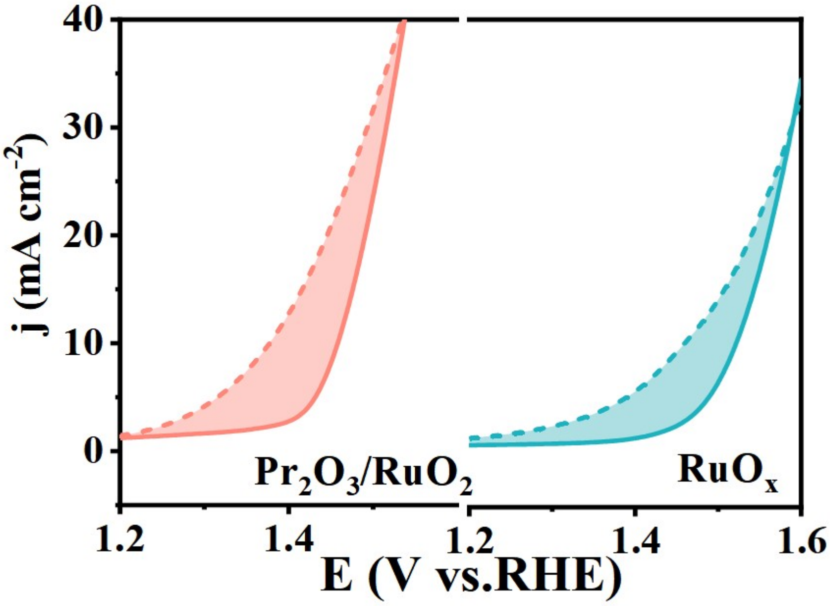

Fig. S25 OER LSV curves of Pr_2O_3/RuO_2 and RuO_x in 0.5 M H_2SO_4 with and without methanol (1.0 M) solution.

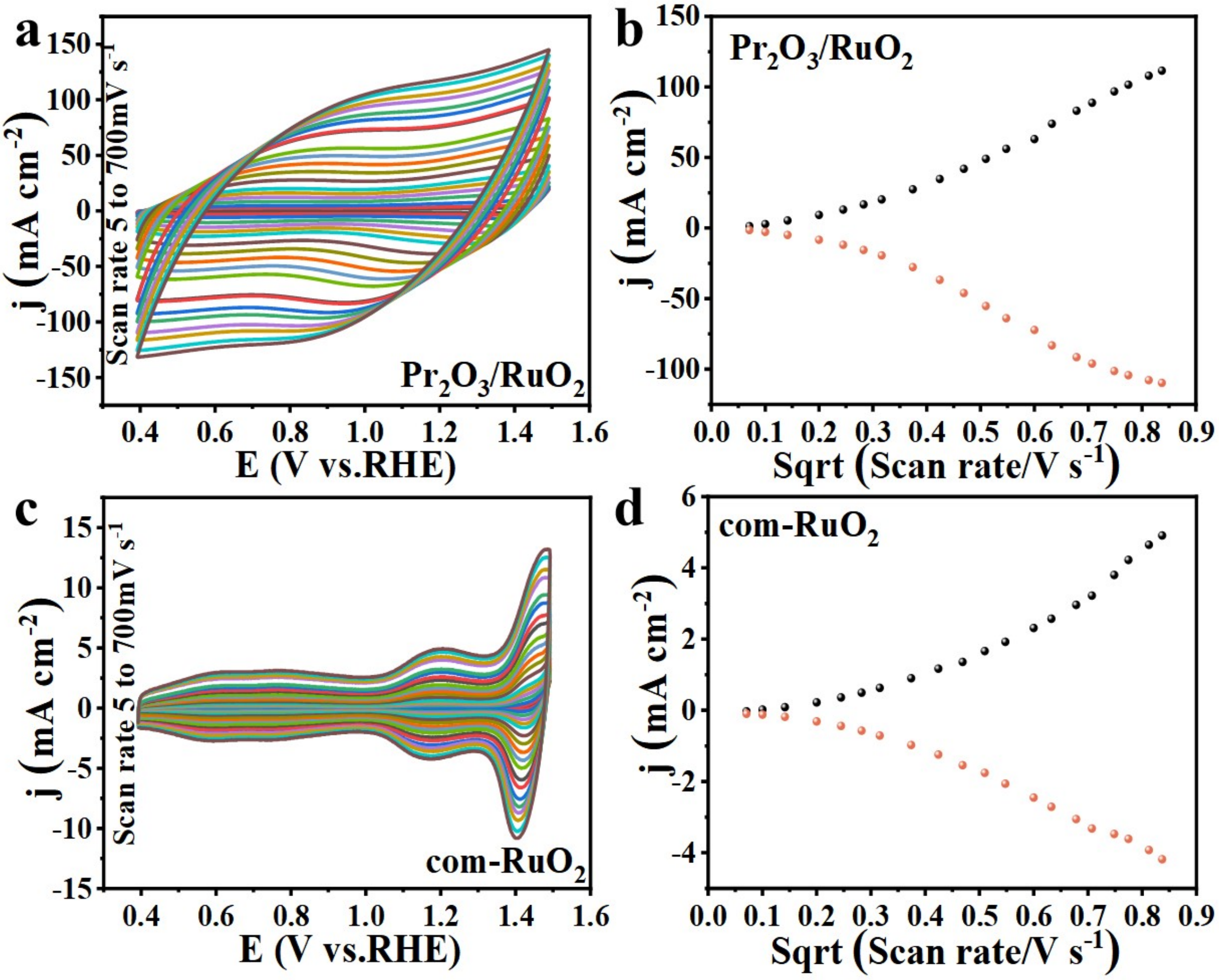

Fig. S26 a) Electrochemical redox coefficients for Pr_2O_3/RuO_2 and c) com-RuO_2; b) Redox currents and square roots of scan rates for Pr_2O_3/RuO_2 and d) com-RuO_2.

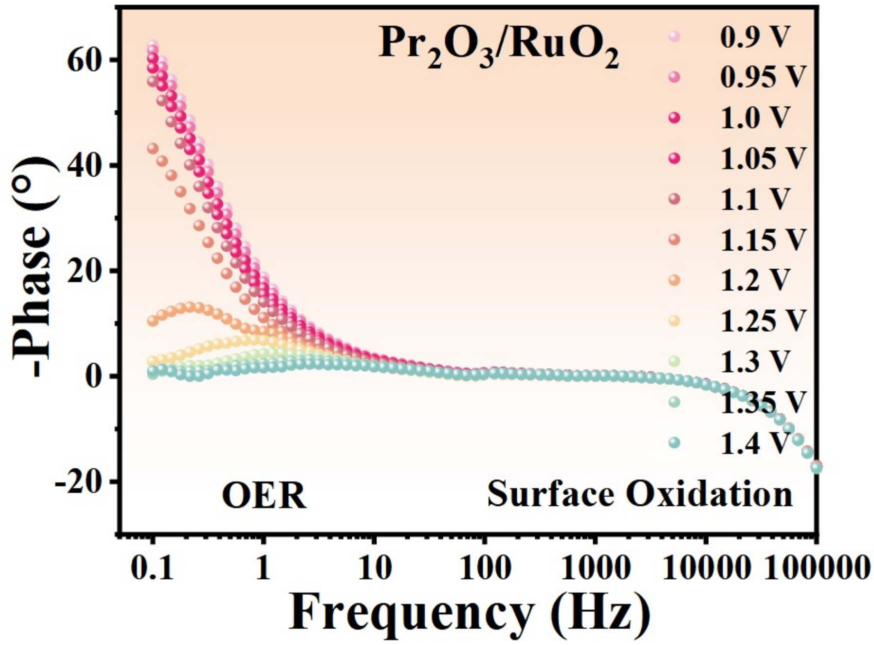

Fig. S27 Bode phase diagram of Pr_2O_3/RuO_2 at defined anodic potentials.

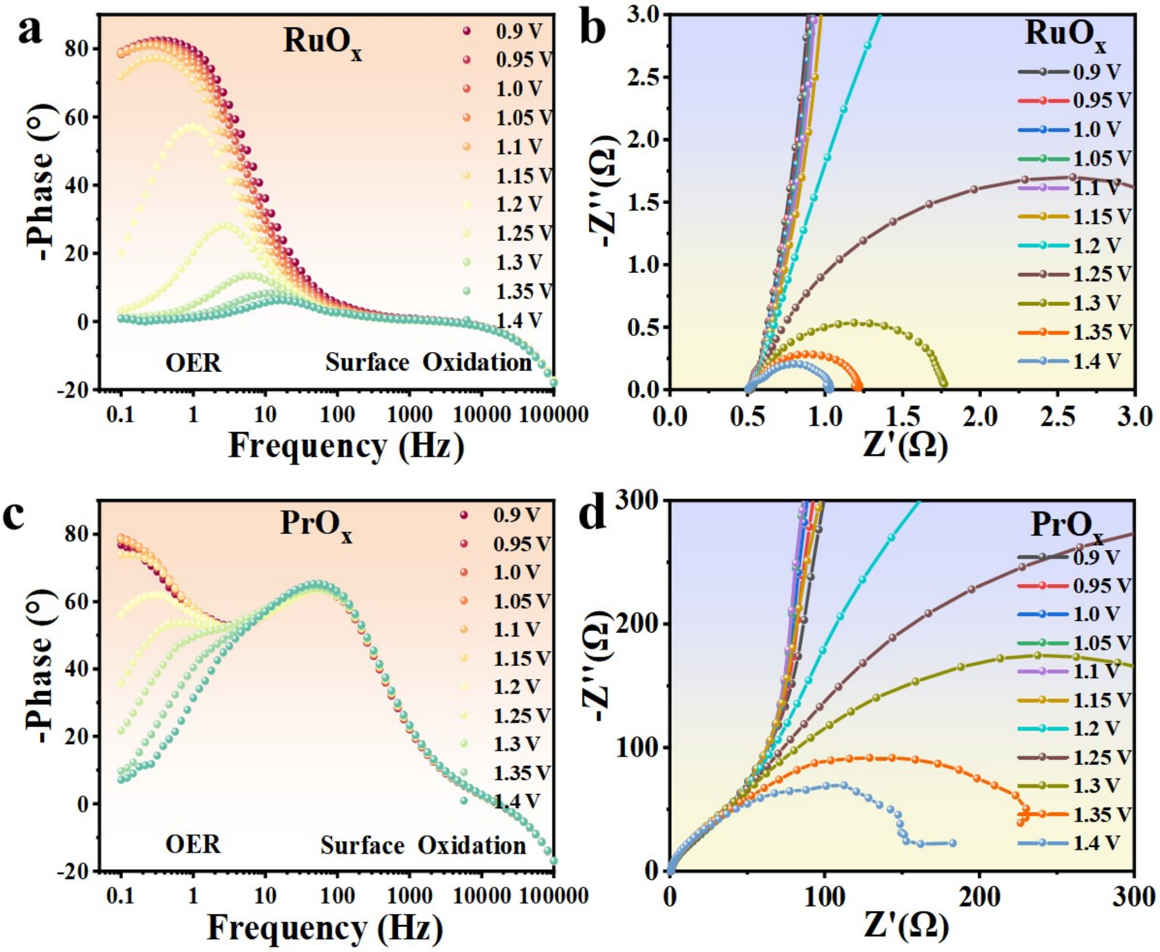

Fig. S28 a-b) Nyquist plots and corresponding Bode absolute impedance plots of Hg/HgO obtained with RuO$_x$; c-d) Nyquist plots and corresponding Bode absolute impedance plots of Hg/HgO obtained with PrO$_x$ at 0.9–1.40 V.

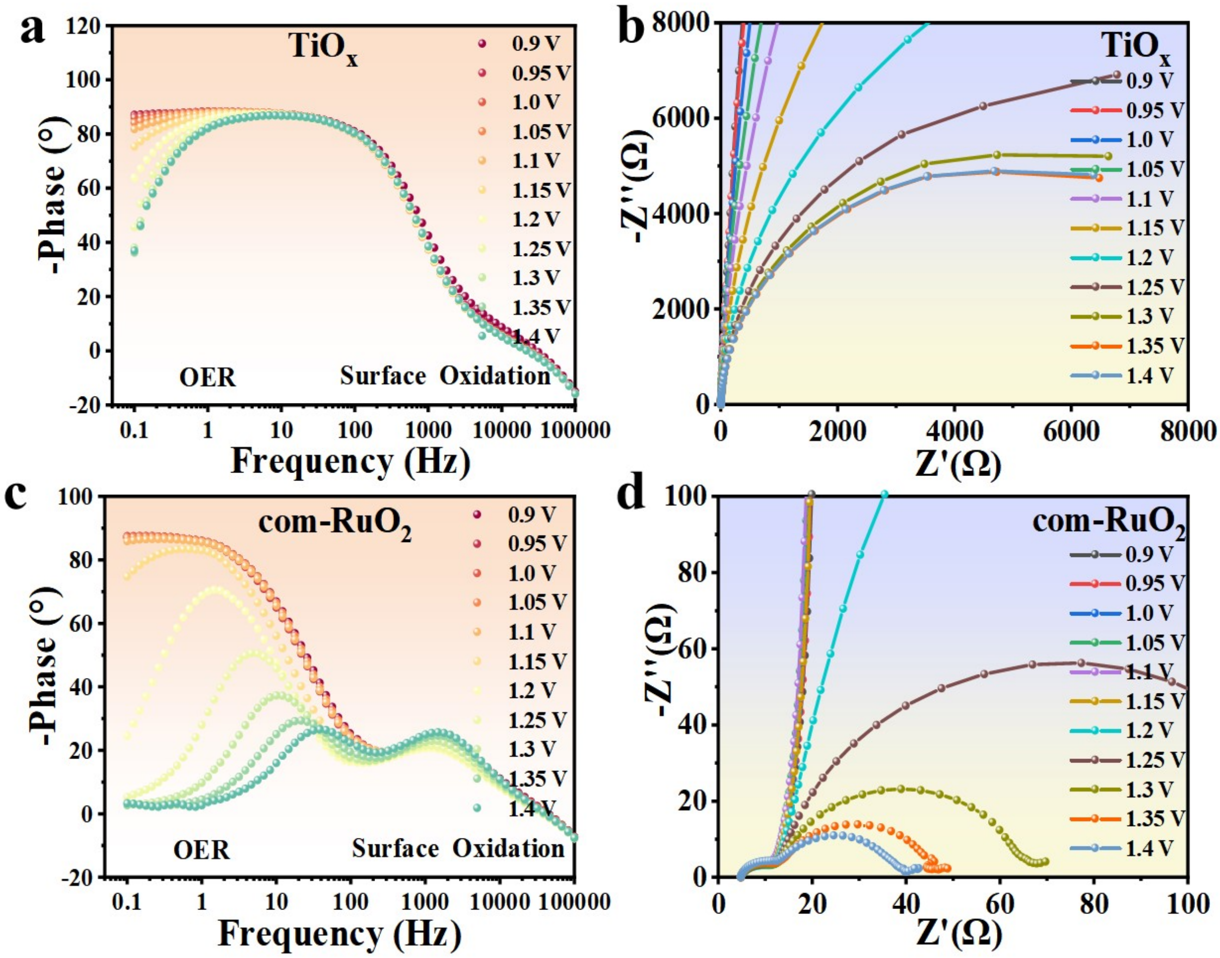

Fig. S29 a-b) Nyquist plots and corresponding Bode plots of absolute impedance for Hg/HgO obtained on TiO$_x$; c-d) Nyquist plots and corresponding Bode plots of absolute impedance for Hg/HgO obtained on com-RuO$_2$ at 0.9–1.40 V.

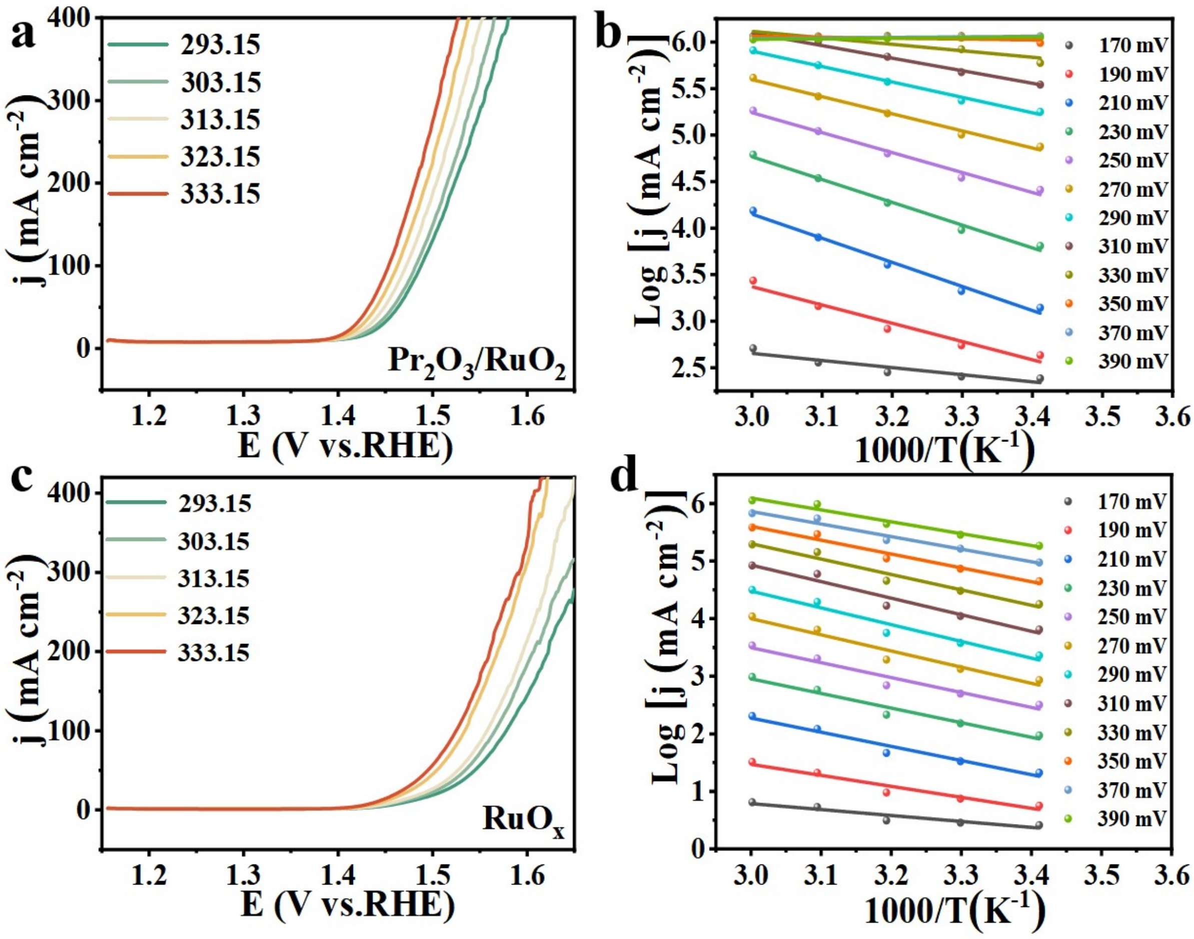

Fig. S30 LSV curves of a) Pr_2O_3/RuO_2 and c) RuO_x measured in 0.5 M H_2SO_4 as a function of temperature, with a scan rate of 10 mV/s. b) and d) Arrhenius plots for Pr_2O_3/RuO_2 and RuO_x at overpotentials of 170, 190, 210, 230, 250, 270, 290, 310, 330, 350, 370, and 390 mV, respectively.

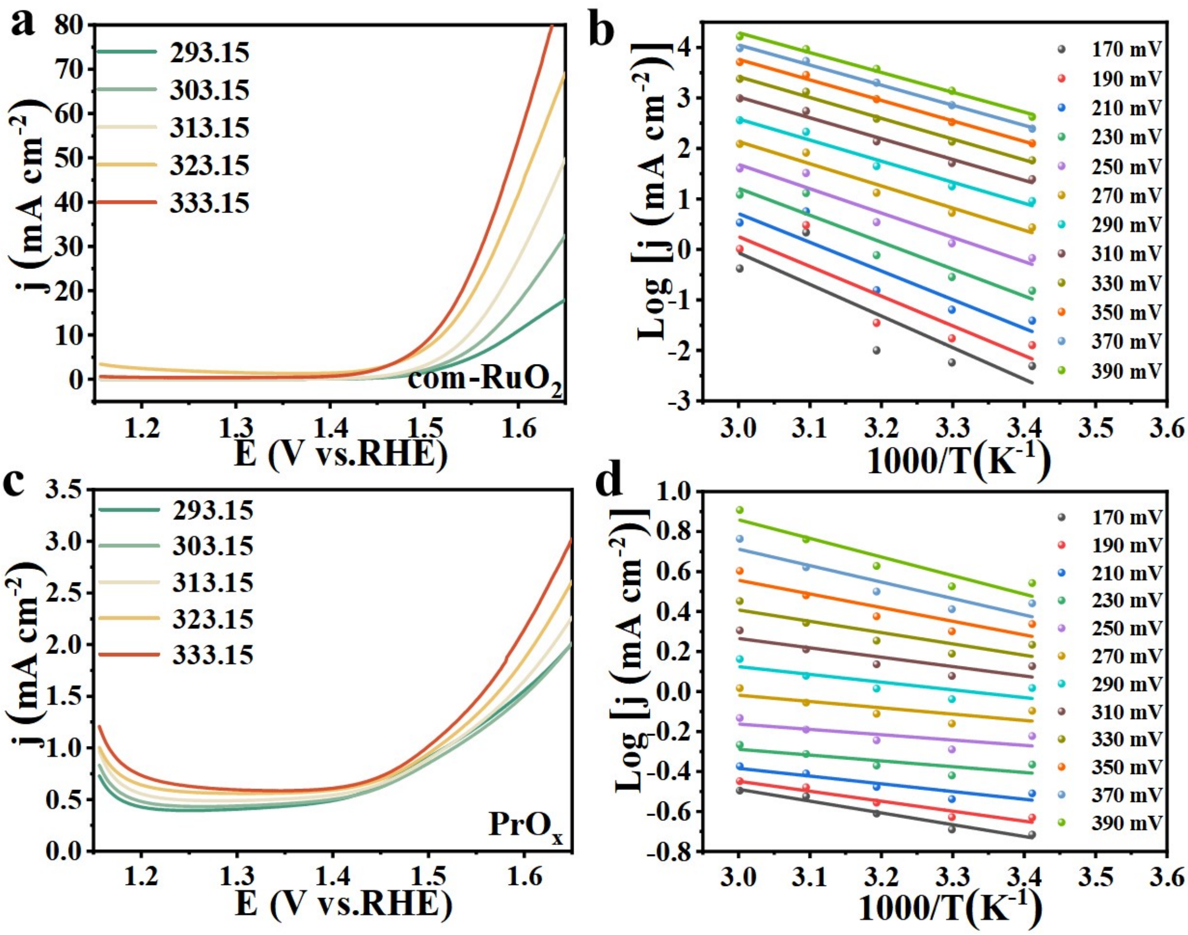

Fig. S31 LSV curves of a) com-RuO$_2$ and c) PrO$_x$ measured in 0.5 M H_2SO_4 as a function of temperature, with a scan rate of 10 mV/s. b) and d) Arrhenius plots for com-RuO$_2$ and PrO$_x$ at overpotentials of 170, 190, 210, 230, 250, 270, 290, 310, 330, 350, 370, and 390 mV, respectively.

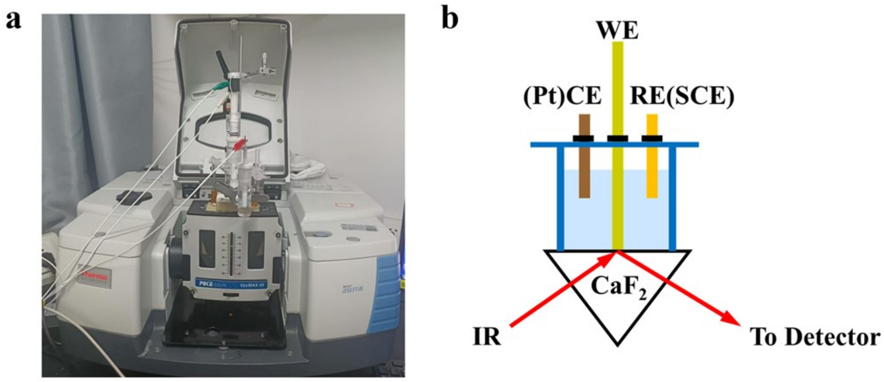

Fig. S32 a) In-situ infrared instrument diagram; b) Schematic of in situ infrared testing.

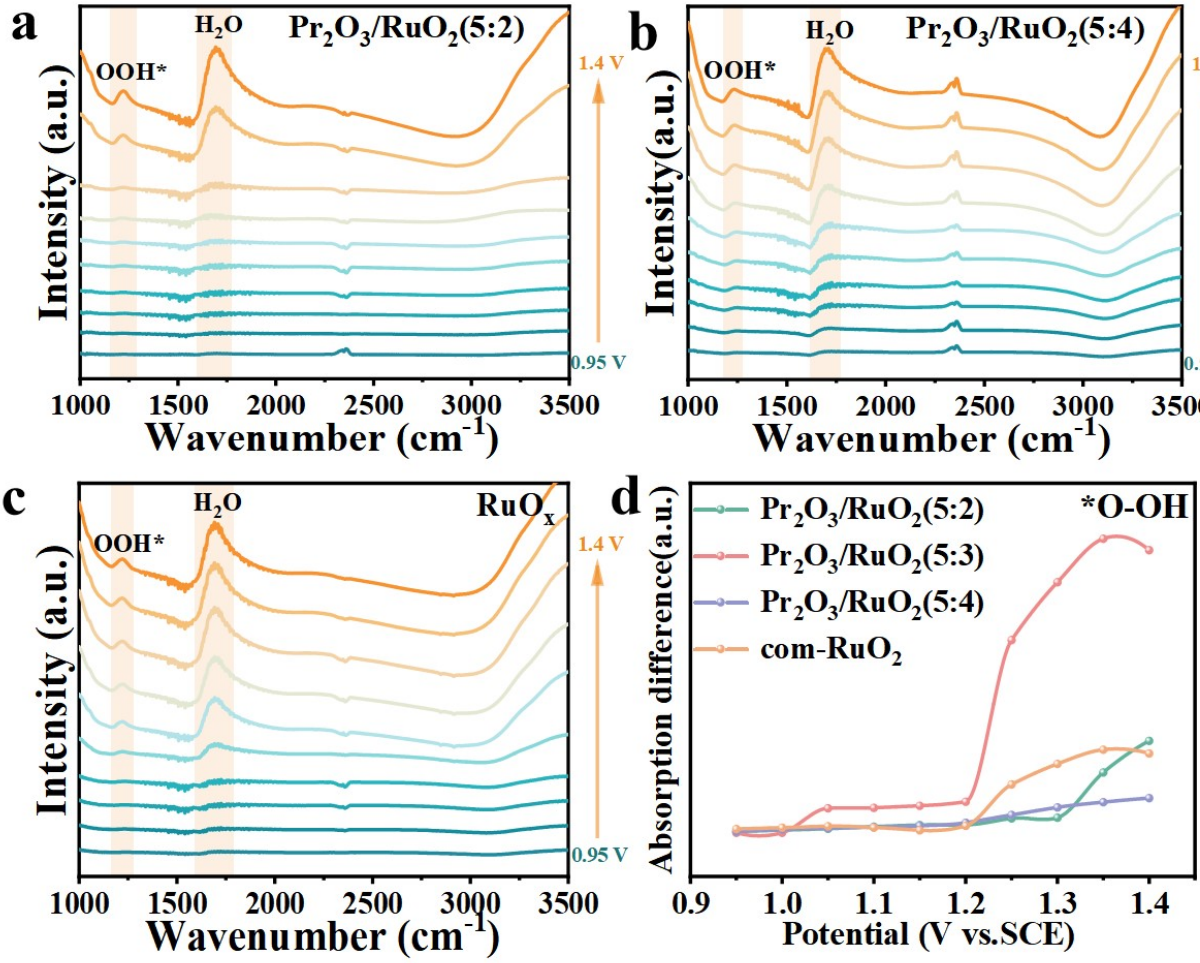

Fig. S33 a) In situ infrared spectra of Pr_2O_3/RuO_2 (5:2), b) Pr_2O_3/RuO_2(5:4), and c) RuO_x; d) Voltage-dependent curve of the peak area for the OOH* intermediate at 1216 cm^{-1}.

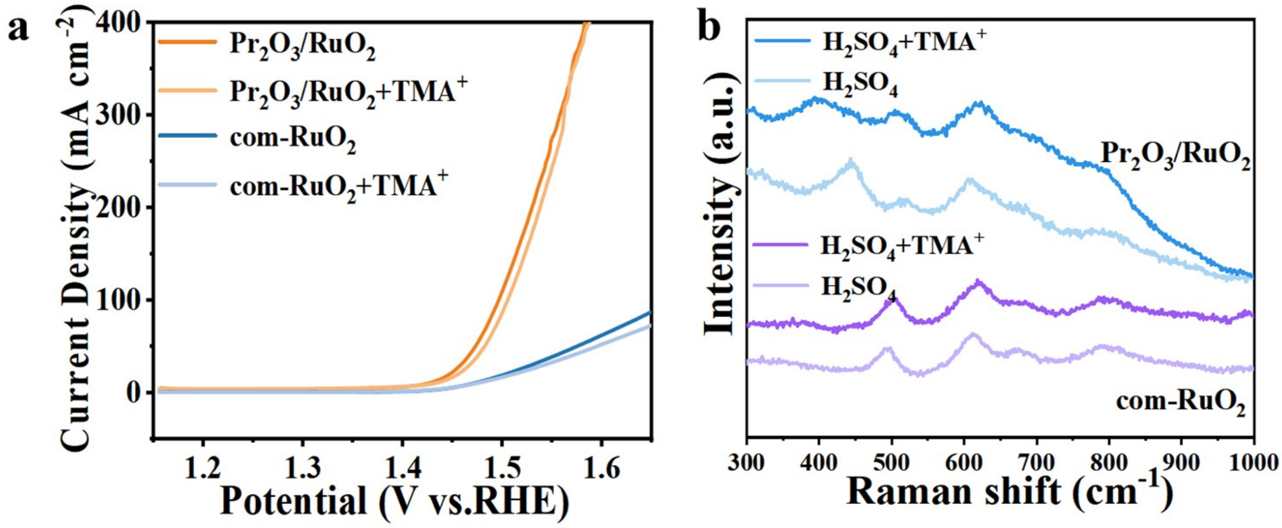

Fig. S34 a) LSV test curves of Pr_2O_3/RuO_2 and com-RuO_2 under TMA^+ conditions; b) Raman test curves of Pr_2O_3/RuO_2 and com-RuO_2 under TMA^+ conditions.

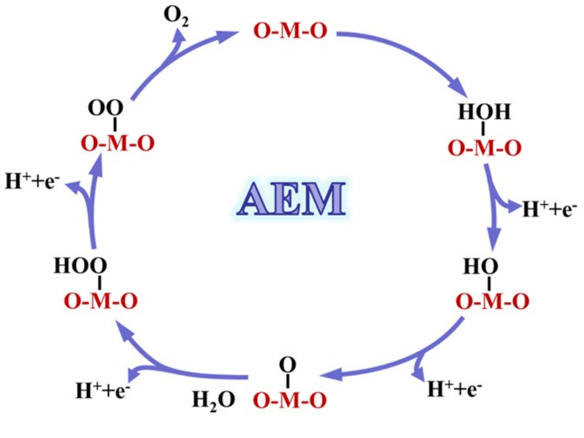

Fig. S35 Mechanism schematic of adsorption evolution mechanism AEM in the OER reaction under acidic conditions.

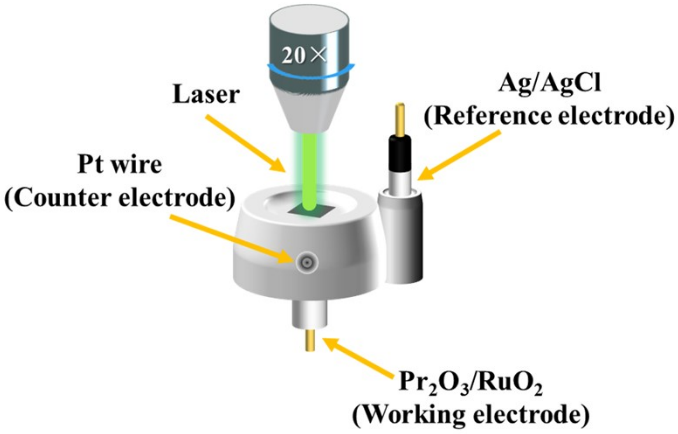

Fig. S36 Schematic diagram of a Raman spectrometer.

Table 1 Performance Comparison with Other Precious Metal Catalysts under Acidic Conditions

Sample	**Electrolyte**	***η*10 (mV)**	**Stability**	**Ref.**
Pr_2O_3/RuO_2	0.5 M H_2SO_4	162	100 h @ 10 mA cm^{-2}	The work
$Nd_{0.1}RuO_x/CC$	0.5 M H_2SO_4	211	50 h @ 10 mA cm^{-2}	2
$RuO_2/Co_3O_4/CC$	0.5 M H_2SO_4	384	24 h @ 10 mA cm^{-2}	3
Li-IrO_x	0.5 M H_2SO_4	270	10 h @ 10 mA cm^{-2}	4
$Rh_{22}Ir_{78}/VXC$	0.5 M H_2SO_4	292	8 h @1.53 V	5
$Pr_2Ru_2O_7$	0.5 M H_2SO_4	213	12 h @ 10 mA cm^{-2}	6
$Y_2Ru_{1.8}Ti_{0.2}O_7$	0.5 M H_2SO_4	229	20 h @ 10 mA cm^{-2}	7
$SRuO_2$-WC NPs	0.5 M H_2SO_4	347	10 h @ 10 mA cm^{-2}	8
RuO_2-NS/CF	0.5 M H_2SO_4	212	50 h @ 10 mA cm^{-2}	9
Co-RuO_2/TiO_2	0.5 M H_2SO_4	266	50 h @ 10 mA cm^{-2}	10
$Ir_{0.3}Ru_{0.7}O_x/C$	0.1 M $HClO_4$	217	40 h @ 10 mA cm^{-2}	11
TNW@RuO_2	0.5 M H_2SO_4	275	24 h @ 10 mA cm^{-2}	12
Ir−$NiCo_2O_4$ NSs	0.5 M H_2SO_4	240	70 h @10 mA cm^{-2}	13
$Ir_1/Cu_{0.3}Co_{2.7}O_4$	0.1 M $HClO_4$	290	60 h @10 mA cm^{-2}	14

Table S2 The amount of dissolved Ru that occupies the total catalyst loadings on the electrode.

Sample	After 1h	After 5h	After 10h	After 25 h	After 50h	After 100h
Pr_2O_3/RuO_2 (Ru)	0%	0%	0%	0.02%	0.04%	0.06%
Pr_2O_3/RuO_2 (Pr)	0%	0%	0%	0%	0.01%	0.02%

References

1 C. C. McCrory, S. Jung, I. M. Ferrer, S. M. Chatman, J. C. Peters and T. F. Jaramillo, *J. Am. Chem. Soc.*, 2015, **137**, 4347-4357.

2 L. Li, G. Zhang, J. Xu, H. He, B. Wang, Z. Yang and S. Yang, *Adv. Funct. Mater.*, 2023, **33**, 2213304.

3 S. Niu, X.-P. Kong, S. Li, Y. Zhang, J. Wu, W. Zhao and P. Xu, *Appl. Catal. B-Environ.*, 2021, **297**, 120442.

4 J. Gao, C.-Q. Xu, S.-F. Hung, W. Liu, W. Cai, Z. Zeng, C. Jia, H. M. Chen, H. Xiao and J. Li, *J. Am. Chem. Soc.*, 2019, **141**, 3014-3023.

5 H. Guo, Z. Fang, H. Li, D. Fernandez, G. Henkelman, S. M. Humphrey and G. Yu, *ACS Nano*, 2019, **13**, 13225-13234.

6 J. Zhang, L. Shi, R. Tong and L. Yang, *ACS Appl. Mater. Interfaces*, 2023, **15**, 52358-52367.

7 N. Zhang, C. Wang, J. Chen and Y. Chai, *EcoMat*, 2023, **5**, e12290.

8 S. C. Sun, H. Jiang, Z. Y. Chen, Q. Chen, M. Y. Ma, L. Zhen, B. Song and C. Y. Xu, *Angew. Chem., Int. Ed.*, 2022, **61**, e202202519.

9 H. Huang, H. Kim, A. Lee, S. Kim, W.-G. Lim, C.-Y. Park, S. Kim, S.-K. Kim and J. Lee, *Nano Energy*, 2021, **88**, 106276.

10 L. Lu, Z. Xu, S. Wei, S. Zhao, X. Du, Y. Wang, L. Wu and G. Liu, *Chem. Eng. J.*, 2024, **500**, 157107.

11 J. S. Zeng, Z. X. Qian, Q. N. Zheng, J. H. Tian, H. Zhang and J. F. Li, *ChemCatChem*, 2024, **16**, e202301222.

12 Y. Liu, T. Duan, L. Xu, X. Gao, L. Xue, Y. Xin, L. Ma, G. Huang and T. Liu, *Int. J. Hydrogen Energy*, 2023, **48**, 10737-10754.

13 J. Yin, J. Jin, M. Lu, B. Huang, H. Zhang, Y. Peng, P. Xi and C.-H. Yan, *J. Am. Chem. Soc.*, 2020, **142**, 18378-18386.

14 Z. Zhang, C. Jia, P. Ma, C. Feng, J. Yang, J. Huang, J. Zheng, M. Zuo, M. Liu and S. Zhou, *Nat. Commun.*, 2024, **15**, 1767.